Generalized ultrastrong optomechanical-like coupling

Jie-Qiao Liao[1,*] Jin-Feng Huang,[1] Lin Tian[2] Le-Man Kuang,[1] and Chang-Pu Sun[3,4]

[1]*Key Laboratory of Low-Dimensional Quantum Structures and Quantum Control of Ministry of Education, Key Laboratory for Matter Microstructure and Function of Hunan Province, Department of Physics and Synergetic Innovation Center for Quantum Effects and Applications, Hunan Normal University, Changsha 410081, China*
[2]*School of Natural Sciences, University of California, Merced, California 95343, USA*
[3]*Beijing Computational Science Research Center, Beijing 100193, China*
[4]*Graduate School of Chinese Academy of Engineering Physics, Beijing 100084, China*

Ultrastrong optomechanical interaction is a significant element for the study of the fundamentals and applications of optomechanical physics, but its realization remains a big challenge in the field of optomechanics. In this work, we propose a reliable scheme to realize a generalized ultrastrong optomechanical-like coupling in a cross-Kerr-type coupled two-bosonic-mode system, in which one of the two bosonic modes is strongly driven. The generalized optomechanical-like interaction takes the form of a product of the excitation number operator of one mode and the rotated quadrature operator of the other mode. Here, both the coupling strength and the phase angle of the rotated quadrature operator are tunable via the driving field. The optomechanical-like coupling can be strongly enhanced to enter the ultrastrong-coupling regime, where the few-photon optomechanical effects such as photon blockade and macroscopic quantum superposition become accessible. The controllability of the quadrature phase angle provides a new degree of freedom for the manipulation of optomechanical systems and enables the implementation of geometric quantum operations. We also present some discussions on the experimental implementation of this scheme. This study will pave the way to the study of quantum physics and quantum technology at the few-photon level in optomechanical systems.
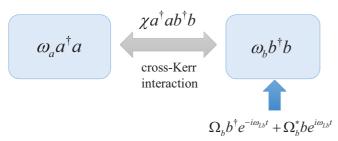
I. INTRODUCTION

Light-matter interaction is at the heart of cavity optomechanics [1–3] and is at the root of various quantum coherence effects in optomechanical systems. The studies of cavity optomechanics focus primarily on the understanding, manipulation, and exploitation of optomechanical couplings and aim to explore both the fundamentals of quantum theory and modern quantum technology. Of particular interest is the study of optomechanics at the few-photon level [4–11]. This is because the nonlinear optomechanical interaction is an intrinsic characteristic of optomechanics. Many interesting effects appear in this regime, such as phonon sideband spectrum [4,6], photon blockade in the cavity driven by a continuous wave [5] or a wave packet [7], and macroscopic quantum coherence [10,11]. However, the few-photon optomechanical effects have not been observed in experiments because the single-photon optomechanical coupling is too weak to be resolved from the environmental noise. How to enhance the optomechanical coupling remains a significant challenge in this field. Until now, people have proposed several methods to enhance the single-photon optomechanical coupling. These methods include the construction of an array of mechanical resonators [12], the use of the nonlinearity in Josephson junctions [13–15], the modulation of the couplings [16], and the utilization of quantum squeezing resources [17,18],

mechanical amplification [19], and delayed quantum feedback [20]. In addition, a proposal has been made to enhance the single-photon optomechanical effect by effectively decreasing the driving detuning of the radiation pressure force [11].

In this paper, we propose an efficient approach to realize a generalized optomechanical-like interaction in the ultrastrong-coupling regime [21–30]. Here, the ultrastrong coupling is referred to the scenario when the strength of the single-photon optomechanical coupling is a considerable fraction of the mechanical frequency [31]. Our scheme is realized by applying a strong driving on one of the two bosonic modes coupled by the cross-Kerr interaction. Note that the cross-Kerr interaction has been widely used in quantum state preparation [32–34], quantum information protocols [35–38], quantum nondemolition photon measurement [39,40], phonon counting [41], and optical devices [42]. In particular, the generalized optomechanical-like coupling takes the form of the product of the occupation number operator of one mode and the quadrature operator of the other mode. Here, the strength of single-photon optomechanical coupling is enhanced by the driving to reach the ultrastrong-coupling regime. Our scheme has the following features: (i) The driving field enhances the optomechanical coupling strength to reach the ultrastrong coupling regime. (ii) The rotated quadrature operator in this generalized optomechanical-like coupling provides a new degree of freedom for the manipulation of optomechanical systems. (iii) This method works for both steady-state and transient displacements, which correspond to constant and modulated optomechanical-coupling cases.

*jqliao@hunnu.edu.cn

FIG. 1. Schematic diagram of the system. Two bosonic modes (a and b) with resonance frequencies ω_a and ω_b are coupled with each other by a cross-Kerr interaction with coupling strength χ. One of the modes (e.g., mode b) is driven by a monochromatic field with the driving frequency ω_{Lb} and driving amplitude Ω_b.

(iv) In the displacement representation (a rotating frame), the driving detuning plays the role of the effective mechanical frequency, which can be much higher than the natural frequency of the mechanical mode and hence suppress its thermal noise.

The rest of this paper is organized as follows: In Sec. II, we introduce the physical model and present the Hamiltonians. In Sec. III, we derive the approximate optomechanical-like Hamiltonian and evaluate the validity of the approximate Hamiltonian. In Secs. IV and V, we study the photon blockade effect in mode a and the generation of the Schrödinger cat states in mode b, respectively. In Sec. VI, we study the geometric quantum operation and the generation of the Schrödinger cat and kitten states in mode a. Some discussions on the experimental implementation of this scheme is present in Sec. VII. Finally, we conclude this work in Sec. VIII.

II. PHYSICAL MODEL

We consider two bosonic modes coupled by a cross-Kerr interaction. One of the two modes (for instance mode b) is driven by a monochromatic field (Fig. 1). The Hamiltonian of the system reads ($\hbar = 1$)

$$H_{\text{sys}} = \omega_a a^\dagger a + \omega_b b^\dagger b + \chi a^\dagger a b^\dagger b$$
$$+ \Omega_b b^\dagger e^{-i\omega_{Lb}t} + \Omega_b^* b e^{i\omega_{Lb}t}, \tag{1}$$

where a ($a^\dagger$) and b ($b^\dagger$) are the annihilation (creation) operators of the two bosonic modes, with the corresponding resonance frequencies ω_a and ω_b. The parameter χ is the coupling strength of the cross-Kerr interaction between the two modes. The mode b is driven by a monochromatic field, with ω_{Lb} and Ω_b being the driving frequency and amplitude, respectively. In a rotating frame with respect to $H_0 = \omega_{Lb} b^\dagger b$, the Hamiltonian becomes

$$H_I = \omega_a a^\dagger a + \Delta_b b^\dagger b + \chi a^\dagger a b^\dagger b + \Omega_b b^\dagger + \Omega_b^* b, \tag{2}$$

where $\Delta_b = \omega_b - \omega_{Lb}$ is the detuning of the resonance frequency ω_b of mode b with respect to the driving frequency ω_{Lb}.

To describe the damping and noise in this system, we assume that the two bosonic modes are coupled to two individual Markovian heat baths, then the quantum master equation

governing the evolution of the system can be written as

$$\dot\rho = i[\rho, H_I] + \gamma_a(\bar n_a + 1)\mathcal{D}[a]\rho + \gamma_a \bar n_a \mathcal{D}[a^\dagger]\rho$$
$$+ \gamma_b(\bar n_b + 1)\mathcal{D}[b]\rho + \gamma_b \bar n_b \mathcal{D}[b^\dagger]\rho, \tag{3}$$

where $\mathcal{D}[o]\rho = o\rho o^\dagger - (o^\dagger o\rho + \rho o^\dagger o)/2$ is a standard Lindblad superoperator for bosonic-mode damping, γ_a (γ_b) and $\bar n_a$ ($\bar n_b$) are the damping rate and environment thermal excitation occupation of mode a (b), respectively.

III. THE GENERALIZED ULTRASTRONG OPTOMECHANICAL-LIKE HAMILTONIAN

In this section, we derive the approximate Hamiltonian: generalized ultrastrong optomechanical-like Hamiltonian and analyze the parameter conditions of the approximation.

A. Derivation of the approximate Hamiltonian

The motivation of this work is to obtain an ultrastrong optomechanical-like coupling between the two modes. Under strong driving, the mode b is excited with a large occupation number, and the operator b can be written as the summation of its mean value and a quantum fluctuation $b \to \beta + b$, and similarly $b^\dagger \to \beta^* + b^\dagger$. Note that the occupation number of mode a is independent of the driving on mode b because the operator $a^\dagger a$ is a conserved quantity. The cross-Kerr interaction then becomes $\chi a^\dagger a(\beta^* + b^\dagger)(\beta + b) = \chi\beta^*\beta a^\dagger a + \chi a^\dagger a(\beta^* b + \beta b^\dagger) + \chi a^\dagger a b^\dagger b$. Here the first term is a frequency shift of mode a, the second term is the generalized optomechanical-like coupling with the coupling strength enhanced by a factor $|\beta|$, and the third term is the cross-Kerr interaction between mode a and the fluctuation of mode b. Below, we present a rigorous derivation of the generalized optomechanical-like Hamiltonian in the open-system case.

In the strong-driving case, the excitation number in mode b is large and then mode b contains a coherent part. This coherent part can be seen by performing the following displacement transformation:

$$\rho' = D_b(\beta)\rho D_b^\dagger(\beta), \tag{4}$$

where ρ' is the density matrix of the two-mode system in the displacement representation, $D_b(\beta) = \exp(\beta b^\dagger - \beta^* b)$ is the displacement operator, and β is the coherent displacement amplitude, which needs to be determined in the transformed quantum master equation. When the coherent displacement amplitude β obeys the equation $\dot\beta + (i\Delta_b + \gamma_b/2)\beta - i\Omega_b = 0$, we can obtain the quantum master equation in the displacement representation as

$$\dot\rho' = i[\rho', H_{\text{tra}}] + \gamma_a(\bar n_a + 1)\mathcal{D}[a]\rho' + \gamma_a \bar n_a \mathcal{D}[a^\dagger]\rho'$$
$$+ \gamma_b(\bar n_b + 1)\mathcal{D}[b]\rho' + \gamma_b \bar n_b \mathcal{D}[b^\dagger]\rho', \tag{5}$$

where the transformed Hamiltonian in the displacement representation reads

$$H_{\text{tra}} = (\omega_a + \chi|\beta|^2)a^\dagger a + (\Delta_b + \chi a^\dagger a)b^\dagger b$$
$$- \chi a^\dagger a(\beta b^\dagger + \beta^* b). \tag{6}$$

Based on the tasks, there are two cases of the displacement: the steady-state displacement and the transient displacement. In the former case, the steady-state displacement amplitude

can be obtained as $\beta_{\text{ss}} = \Omega_b/(\Delta_b - i\gamma_b/2)$, which indicates that the displacement amplitude β_{ss} is tunable by choosing proper parameters Ω_b and Δ_b. The value of $|\beta_{\text{ss}}|$ could be much larger than 1 in the strong-driving case $\Omega_b \gg \{\Delta_b, \gamma_b\}$. For the transient-solution case, the optomechanical-like coupling becomes a time-dependent interaction. In particular, the interaction strength $g_0(t) = \chi\beta(t)$ is tailorable because we can obtain a desired $\beta(t)$ by designing a proper driving amplitude $\Omega_b(t)$. For example, we can choose $\Omega_b(t)$ such that a sinusoidal enhancement $g_0 \sin(\omega_d t)$ is obtained, where ω_d is the modulation frequency. It has been proved that the modulated optomechanical coupling can be used to enhance the photonic nonlinearity and to generate macroscopic superposition states [16].

In this work, we mainly focus on the steady-state displacement case, in which the timescale of the system approaching to its steady state is much shorter than other evolution timescales. In this case, the Hamiltonian becomes

$$H_{\text{tra}} = \omega_a' a^\dagger a + (\Delta_b + \chi a^\dagger a)b^\dagger b - g_0 a^\dagger a(b^\dagger e^{i\theta} + be^{-i\theta}),$$
(7)

where we introduce the normalized frequency $\omega_a' = \omega_a + \chi|\beta_{\text{ss}}|^2$, the enhanced coupling strength

$$g_0 = \chi|\beta_{\text{ss}}|,$$
(8)

and the phase angle θ of the quadrature operator of mode b, which is defined by $\beta_{\text{ss}} = |\beta_{\text{ss}}|e^{i\theta}$.

The motivation for realization of the ultrastrong optomechanics is to study the few-photon physics in optomechanical systems, therefore we will focus on the few-photon regime in the following. Under the condition

$$|m\chi| \ll \Delta_b,$$
(9)

with m being the largest excitation number involved in mode a, we can neglect the cross-Kerr interaction term in Eq. (7) to obtain the approximate Hamiltonian as

$$H_{\text{app}} = \omega_a' a^\dagger a + \Delta_b b^\dagger b - g_0 a^\dagger a(b^\dagger e^{i\theta} + be^{-i\theta}).$$
(10)

This approximate Hamiltonian is the main result of this work. Here we can see that the effective frequency of mode b is given by Δ_b, and that the effective coupling strength of the generalized optomechanical-like coupling is given by $g_0 \equiv \chi|\beta_{\text{ss}}|$. The effective frequency Δ_b is controllable by tuning the driving frequency ω_{Lb}, and the generalized coupling strength could be largely enhanced to enter the ultrastrong-coupling regime by choosing a proper driving amplitude Ω_b. The form of the optomechanical-like coupling is generalized because this coupling takes the form of a product of the occupation number operator of mode a and the quadrature operator of mode b. The quadrature angle θ can be tuned by choosing the driving frequency ω_{Lb} and amplitude Ω_b.

B. Evaluation of the validity of the approximate Hamiltonian

In the derivation of the approximate Hamiltonian H_{app}, the only approximation is the omission of the cross-Kerr interaction term in the transformed Hamiltonian H_{tra} in Eq. (7). The condition under which the approximation is justified is that the frequency shift of mode b induced by the cross-Kerr interaction should be much smaller than its effective frequency

Δ_b in the displacement representation. Below, we evaluate the validity of this approximation by calculating the fidelity between the exact state and the approximate state. To avoid the crosstalk from the dissipations, we first consider the closed-system case, in which the evolutions of the exact state and the approximate state are governed by the exact Hamiltonian H_{tra} and the approximate Hamiltonian H_{app}, respectively. We assume that the initial state of the system is $|\psi(0)\rangle = |m\rangle_a|0\rangle_b$ so that we can calculate the exact state and the approximate state analytically. Here $|m\rangle_a$ and $|0\rangle_b$ are the Fock states for modes a and b, respectively.

Based on the exact Hamiltonian (7), the exact state of the system at time t can be obtained as

$$|\psi_{\text{ext}}(t)\rangle = e^{-im\omega_a' t}e^{i\zeta(t)}|m\rangle_a|\eta(t)\rangle_b,$$
(11)

where the phase and the displacement amplitude are defined by

$$\zeta(t) = \frac{m^2\chi^2|\beta_{\text{ss}}|^2}{(\Delta_b + m\chi)^2}[(\Delta_b + m\chi)t - \sin[(\Delta_b + m\chi)t]],$$
(12)

and

$$\eta(t) = \frac{m\chi\beta_{\text{ss}}}{(\Delta_b + m\chi)}(1 - e^{-i(\Delta_b + m\chi)t}).$$
(13)

Similarly, the approximate state of the system at time t can be obtained, in terms of the approximate Hamiltonian (10), as

$$|\psi_{\text{app}}(t)\rangle = e^{-im\omega_a' t}e^{i\zeta'(t)}|m\rangle_a|\eta'(t)\rangle_b.$$
(14)

The phase and the displacement amplitude in this case are defined by

$$\zeta'(t) = \frac{m^2\chi^2|\beta_{\text{ss}}|^2}{\Delta_b^2}[\Delta_b t - \sin(\Delta_b t)],$$
(15)

and

$$\eta'(t) = \frac{m\chi\beta_{\text{ss}}}{\Delta_b}(1 - e^{-i\Delta_b t}).$$
(16)

The fidelity between the exact state $|\psi_{\text{ext}}(t)\rangle$ and the approximate state $|\psi_{\text{app}}(t)\rangle$ can be calculated as

$$F(t) = |\langle\psi_{\text{app}}(t)|\psi_{\text{ext}}(t)\rangle|$$
$$= \exp\left[-\frac{1}{2}\left|\frac{m\chi\beta_{\text{ss}}}{\Delta_b}(1 - e^{-i\Delta_b t})\right.\right.$$
$$\left.\left. - \frac{m\chi\beta_{\text{ss}}}{(\Delta_b + m\chi)}(1 - e^{-i(\Delta_b + m\chi)t})\right|^2\right].$$
(17)

For investigating the fidelity in single-photon physical effects, we choose the initial state of the system as $|\psi(0)\rangle = |1\rangle_a|0\rangle_b$. In Fig. 2(a), we show the fidelity $F(t)$ for $m = 1$ and $\theta = 0$ as a function of the evolution time t when $\chi/\Delta_b = 0.005$ and $|\beta_{\text{ss}}| = 100, 500,$ and 1000. We see that the fidelity decreases for larger values of $|\beta_{\text{ss}}|$. This can be explained from the expression of $F(t)$ that the exponential decreasing rate is proportional to $|\beta_{\text{ss}}|^2$ in this case. Nevertheless, the fidelity can be very high because of $\chi \ll \Delta_b$. In Fig. 2(b), we display the fidelity $F(t_s)$ at time $t_s = \pi/\Delta_b$ (the time for generation of cat states in mode b) as a function of $|\beta_{\text{ss}}|$ and χ/Δ_b. Here the fidelity is large in a wide parameter space and it is higher
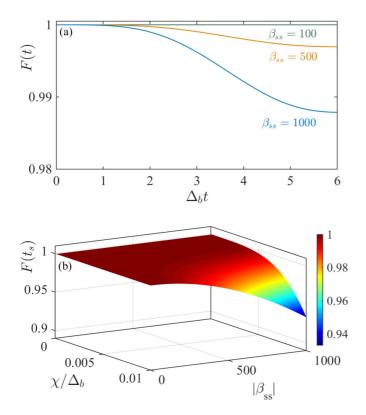
FIG. 2. (a) The fidelity $F(t)$ as a function of the evolution time $\Delta_b t$ when $\chi/\Delta_b = 0.005$ and $|\beta_{ss}| = 100$, 500, and 1000, which correspond to $g_0/\Delta = 0.5$, 2.5, and 5, respectively. (b) The fidelity $F(t_s)$ at time $t_s = \pi/\Delta_b$ as a function of the parameters $|\beta_{ss}|$ and χ/Δ_b.

for a smaller χ/Δ_b. For a given value of χ/Δ_b, the fidelity F is higher for a smaller value of $|\beta_{ss}|$. With the parameters for creating moderate displacement, for example $\chi|\beta_{ss}| = \Delta_b$, the fidelity could be larger than 0.99. Note that this fidelity is independent of ω'_a because the term $\omega'_a a^\dagger a$ commutes with other terms in the Hamiltonian.

Below, we investigate the fidelity when the dissipations are present. In this case, the evolutions of the exact state and the approximate state are, respectively, governed by the exact master equation (5) and the approximation master equation, which takes the same form as Eq. (5) under the replacement $H_{\text{tra}} \rightarrow H_{\text{app}}$. In our simulations, we introduce a parameter η into the equation of motion by the replacement $\chi \rightarrow \eta\chi$ in the last term in Eq. (6) so that we can describe the equations of motion for the density-matrix elements in a unified form. The values of $\eta = 1$ and $\eta = 0$ correspond to the exact- and approximate-solution cases, respectively. By expressing the density matrix of the two-mode system in the number-state representation as

$$\rho' = \sum_{m,j,n,k=0}^{\infty} \rho'_{m,j,n,k} |m\rangle_a |j\rangle_b \, _a\langle n|_b\langle k|, \qquad (18)$$

with $\rho'_{m,j,n,k} = {}_a\langle m|_b\langle j|\rho'|n\rangle_a|k\rangle_b$ being the density-matrix elements, we can obtain the equations of motion for the density-matrix elements based on the quantum master equation.

Based on the initial conditions, we can solve the equations of motion for these density-matrix elements. Without loss of

generality, in the simulations we assume that the initial state of the system is $|\alpha\rangle_a \otimes |\beta\rangle_b$, where $|\alpha\rangle$ and $|\beta\rangle$ are coherent states, then we have

$$\rho'_{m,j,n,k}(0) = e^{-|\alpha|^2} e^{-|\beta|^2} \frac{\alpha^m \alpha^{*n} \beta^j \beta^{*k}}{\sqrt{m!j!n!k!}}. \qquad (19)$$

We denote the density matrices corresponding to the two cases of $\eta = 1$ and $\eta = 0$ as ρ_{ext} and ρ_{app}, respectively, then the fidelity between the exact density matrix ρ_{ext} and the approximate density matrix ρ_{app} can be calculated by

$$F = \text{Tr}\left[\sqrt{\sqrt{\rho_{\text{ext}}}\rho_{\text{app}}\sqrt{\rho_{\text{ext}}}}\right]. \qquad (20)$$

In Fig. 3, we plot the fidelity given by Eq. (20) as a function of the evolution time in the open-system case. Here we choose the initial state of the system as either $|1\rangle_a|0\rangle_b$ or $|\alpha\rangle_a|\beta\rangle_b$. In addition, we choose the parameters as $\chi/\Delta_b = 0.001$, 0.01, and 0.1. The value of the displacement amplitude $|\beta_{\text{ss}}|$ is chosen such that $\chi|\beta_{\text{ss}}| = \Delta_b$. We can see that the fidelity is larger for a smaller value of the ratio χ/Δ_b, which is in consistent with the analysis on the parameter condition of the approximation. Owing to the dissipations, the fidelity experiences some oscillations and then approaches gradually to a stationary value. For a given value of χ, the fidelity approaches to its stationary value in a faster manner for a larger decay rate. When $\bar{n}_a = \bar{n}_b = 0$, the fidelity approaches to 1 in the long-time limit because the steady state of the system is $|0\rangle_a|0\rangle_b$ when it is governed by the quantum master equation (5) with either the exact or approximate Hamiltonian. It can be seen from quantum master equation (5) that the average photon number experiences an exponential decay governed by the equations of motion $d\langle n_a\rangle/dt = -\gamma_a\langle n_a\rangle$. As a result, the steady state of the mode b is $|0\rangle_b$ because mode b is reduced to a free cavity field coupled to a vacuum bath in this case.

IV. PHOTON BLOCKADE EFFECT IN MODE a

One important application of the optomechanical interaction in the ultrastrong-coupling regime is the realization of photon blockade effect [5,7]. The physical mechanism for the creation of the photon blockade effect is the anharmonicity in the eigenenergy spectrum of the optomechanical system. In the generalized optomechanical-like model, the Kerr nonlinearity for mode a can be obtained by diagonalizing the approximate Hamiltonian H_{app} as $V^\dagger H_{\text{app}} V = \omega'_a a^\dagger a + \Delta_b b^\dagger b - (g_0^2/\Delta_b)a^\dagger a a^\dagger a$, using the transformation operator $V = \exp[g_0/\Delta_b a^\dagger a(b^\dagger e^{i\theta} - b e^{-i\theta})]$. To observe the photon blockade effect, the magnitude of the self-Kerr nonlinearity should be much larger than the decay rate of mode a, namely $g_0^2/\Delta_b \gg \gamma_a$, such that the anharmonicity in the energy levels can be resolved from the cavity field linewidth. In our scheme, the Kerr nonlinearity can be enhanced by a large coherent displacement $|\beta_{\text{ss}}|$ and a small driving detuning Δ_b. Here we should point out that a small detuning will not affect the thermal occupation number $\bar{n}_b$ which is determined by the natural resonance frequency ω_b of mode b.

To generate photons in this system, a weak field is introduced to drive mode a. In addition, a strong driving is performed on mode b to enhance the optomechanical coupling.
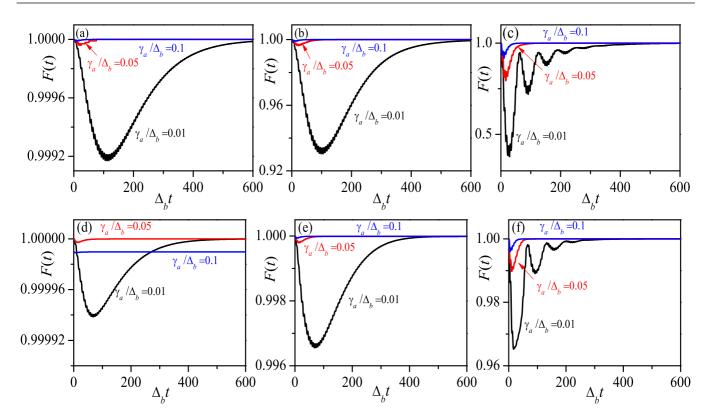
FIG. 3. The dynamics of the fidelity defined by Eq. (20) between the exact state and the approximate state in the open-system case, when the parameter χ takes different values: (a), (d) $\chi/\Delta_b = 0.001$; (b), (e) $\chi/\Delta_b = 0.01$; and (c), (f) $\chi/\Delta_b = 0.1$. Here, the parameter $|\beta_{ss}|$ is chosen such that $\chi|\beta_{ss}| = \Delta_b$. We choose the initial state of the two modes as (a)–(c) $|1\rangle_a|0\rangle_b$ and (d)–(f) $|\alpha_0\rangle_a|\beta_0\rangle_b$ with $\alpha_0 = \beta_0 = 0.2$. We take $\omega_a' = 0$ because the fidelity is independent of this variable ω_a'. The other parameters are given by $\bar{n}_a = \bar{n}_b = 0$.

Then the Hamiltonian of the system can be written as

$$H' = H_{sys} + \Omega_a a^\dagger e^{-i\omega_{La}t} + \Omega_a^* a e^{i\omega_{La}t}, \tag{21}$$

where Ω_a and ω_{La} are the driving amplitude and frequency of mode a. For observation of photon blockade, the driving field on mode a is weak, i.e., $\Omega_a/\gamma_a \ll 1$. For enhancement of the optomechanical coupling, the driving of mode b is strong. i.e., $\Omega_b/\gamma_b \gg 1$. Then we treat the driving on mode a as a perturbation in our calculations.

In a rotating frame with respect to $H_0' = \omega_{La}a^\dagger a + \omega_{Lb}b^\dagger b$, Hamiltonian (21) becomes

$$H_I' = \Delta_a a^\dagger a + \Delta_b b^\dagger b + (\Omega_b b^\dagger + \Omega_b^* b) + \chi a^\dagger a b^\dagger b$$
$$+ (\Omega_a a^\dagger + \Omega_a^* a), \tag{22}$$

where $\Delta_a = \omega_a - \omega_{La}$ is introduced. Using the same method in Sec. III, we add the dissipation terms of the two modes a and b into the quantum master equation. Since the driving on mode a is weak and the driving on mode b is strong, then we only perform the displacement transformation on mode b as $\rho' = D_b(\beta)\rho D_b^\dagger(\beta)$. Based on the fact that the displacement transformation operator commutes with the driving term of mode a, then the quantum master equation in the displacement representation reads

$$\dot{\rho}' = i[\rho', H_{tra}'] + \gamma_a(\bar{n}_a + 1)\mathcal{D}[a]\rho' + \gamma_a\bar{n}_a\mathcal{D}[a^\dagger]\rho'$$
$$+ \gamma_b(\bar{n}_b + 1)\mathcal{D}[b]\rho' + \gamma_b\bar{n}_b\mathcal{D}[b^\dagger]\rho', \tag{23}$$

where the transformed Hamiltonian reads ($\theta = 0$)

$$H_{tra}' = H_{gop}' + (\Omega_a a^\dagger + \Omega_a^* a), \tag{24}$$

with the undriven Hamiltonian

$$H_{gop}' = \Delta_a' a^\dagger a + (\Delta_b + \chi a^\dagger a)b^\dagger b - g_0 a^\dagger a(b^\dagger + b). \tag{25}$$

Here we introduce the driving detuning $\Delta_a' = \omega_a' - \omega_{La}$ for mode a. Then the eigensystem of the Hamiltonian H_{gop}' can be obtained as

$$H_{gop}'|m\rangle_a|\tilde{j}(m)\rangle_b = E_{m,j}'|m\rangle_a|\tilde{j}(m)\rangle_b, \tag{26}$$

where the eigenvalues are given by

$$E_{m,j}' = \Delta_a' m + (\Delta_b + m\chi)j - \frac{g_0^2 m^2}{(\Delta_b + \chi m)}, \tag{27}$$

and the photon-number-dependent displaced Fock states of mode b are defined by

$$|\tilde{j}(m)\rangle_b = \exp\left[\frac{g_0 m}{(\Delta_b + \chi m)}(b^\dagger - b)\right]|j\rangle_b. \tag{28}$$

Equation (27) shows the photonic nonlinearity in the eigenenergy spectrum, and this nonharmonicity in the energy spectrum is the physical origin of the appearance of photon blockade. In our numerical simulations, we solve quantum master equation (23) and obtain the steady state of the system. By calculating the equal-time second-order correlation
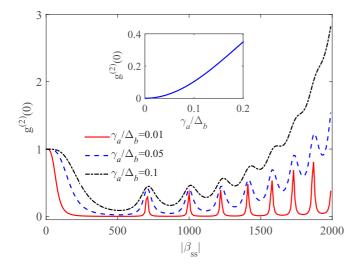
FIG. 4. The equal-time second-order correlation function $g^{(2)}(0)$ of mode a as a function of $|\beta_{ss}|$ when $\gamma_a/\Delta_b = \gamma_b/\Delta_b = 0.01$, 0.05, and 0.1 and under the single-photon resonance driving $\Delta'_a = g_0^2/(\Delta_b + \chi)$. Other parameters used are $\chi/\Delta_b = 0.001$, $\bar{n}_a = \bar{n}_b = 0$, and $\Omega_a/\gamma_a = 0.1$. The inset shows the correlation function $g^{(2)}(0)$ at $g_0/\Delta_b = 0.5$ as a function of γ_a/Δ_b.

function

$$g^{(2)}(0) = \frac{\langle a^\dagger a^\dagger a a \rangle_{ss}}{\langle a^\dagger a \rangle_{ss}^2} \tag{29}$$

in the steady state, we can evaluate the photon blockade effect in this system.

In Fig. 4, we plot the equal-time second-order correlation function as a function of the enhanced factor $|\beta_{ss}|$ at various values of γ_a/Δ_b. Here the operator averages are taken over the steady state of the system [43]. We can see that the photon blockade effect (corresponding to $g^{(2)}(0) \ll 1$) can be observed in the resolved-sideband limit $\gamma_a/\Delta_b \ll 1$. The decay of mode a will harm the photon blockade effect, as shown in the inset, where we display $g^{(2)}(0)$ as a function of γ_a/Δ_b at $g_0/\Delta_b = 0.5$, which corresponds to the optimal $|\beta_{ss}|$ for photon blockade.

To show the dependence of the correlation function $g^{(2)}(0)$ on the system parameters in a wide parameter space, in Fig. 5 we plot the correlation function $g^{(2)}(0)$ of mode a as a function of the displacement amplitude $|\beta_{ss}|$ and the decay rate γ_a/Δ_b. Here we choose the driving detuning $\Delta_a = (\chi|\beta_{ss}|)^2/(\Delta_b + \chi)$ (determined by $E'_{1,0} - E'_{0,0} = 0$) such that the first-photon transition $|0\rangle_a|\tilde{0}(0)\rangle_b \leftrightarrow |1\rangle_a|\tilde{0}(1)\rangle_b$ is resonant. We can see that the correlation function $g^{(2)}(0)$ increases with the increase of the decay rate γ_a. For a small decay rate γ_a, the correlation function $g^{(2)}(0)$ exhibits some resonance peaks, which are induced by the phonon-sideband resonant transitions. In some parameter regions (the valley region) where the first photon transition is resonant and the second-photon transition is far off resonance, then mode a will exhibit the photon blockade effect.

The thermal noise of the environment of mode b will affect the photon blockade effect in mode a. This point can be seen by calculating the equal-time second-order correlation function $g^{(2)}(0)$ in the steady state of the quantum master
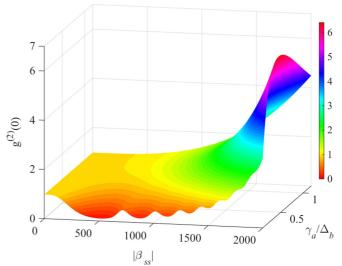

FIG. 5. Plot of equal-time second-order correlation function $g^{(2)}(0)$ as a function of displacement amplitude $|\beta_{ss}|$ and decay rate γ_a/Δ_b. The driving detuning $\Delta_a = (\chi\beta_{ss})^2/(\Delta_b + \chi)$ is chosen such that the single-photon transition is resonant. Other parameters are given by $\chi/\Delta_b = 0.001$, $\gamma_b = \gamma_a$, $\bar{n}_a = \bar{n}_b = 0$, and $\Omega_a/\gamma_a = 0.2$.

equation. In Fig. 6, we show the correlation function $g^{(2)}(0)$ as a function of $|\beta_{ss}|$ when the thermal occupation number takes different values $\bar{n}_b = 5$, 8, and 12. Here we choose different values of the decay rate of mode b: $\gamma_b/\Delta_b = 0.001$ in Fig. 6(a) and $\gamma_b/\Delta_b = 0.01$ in Fig. 6(b). We can see that the lower envelope of the correlation function will increase with the increase of the thermal occupation number $\bar{n}_b$. This means that the thermal noise will harm the photon blockade effect. For a small decay rate $\gamma_b/\Delta_b = 0.001$, the photon blockade effect still exists for a moderately large thermal occupation number $\bar{n}_b$. For a larger value of $\gamma_b/\Delta_b = 0.01$, the photon blockade effect in the large region of $|\beta_{ss}|$ will disappear gradually with the increase of the thermal occupation number $\bar{n}_b$.

V. GENERATION OF THE SCHRÖDINGER CAT STATES IN MODE b

The optomechanical interaction in the ultrastrong-coupling regime can be used to generate the Schrödinger cat states [10] in mode b. In this section, we show the generation of the Schrödinger cat states of mode b by utilizing the generalized optomechanical-like coupling. We start our discussion by considering the Hamiltonian H_{app} given by Eq. (10). In the rotating frame with respect to $H_{app}^{(0)} = \omega'_a a^\dagger a + \Delta_b b^\dagger b$, the Hamiltonian H_{app} becomes

$$H_{app}^{(I)}(t) = -g_0 a^\dagger a (b^\dagger e^{i\Delta_b t} e^{i\theta} + b e^{-i\Delta_b t} e^{-i\theta}). \tag{30}$$

The unitary evolution operator associated with the Hamiltonian H_{app} can be expressed as

$$U(t) = e^{-iH_{app}^{(0)} t} U_{app}(t), \tag{31}$$

where $U_{app}(t)$ is the unitary evolution operator associated with the Hamiltonian $H_{app}^{(I)}(t)$. It takes the form $U_{app}(t) = \mathcal{T} \exp[-i \int_0^t H_{app}^{(I)}(t') dt']$, where "$\mathcal{T}$" denotes the time-ordering integral. The $U_{app}(t)$ is determined by the
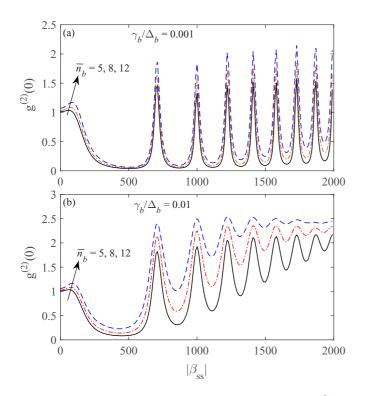
FIG. 6. The equal-time second-order correlation function $g^{(2)}(0)$ of mode a as a function of $|\beta_{ss}|$ when $\bar{n}_b = 5$, 8, and 12. Here we choose different values of the decay rate of mode b: $\gamma_b/\Delta_b = 0.001$ in panel (a) and $\gamma_b/\Delta_b = 0.01$ in panel (b). The driving detuning $\Delta_a' = g_0^2/(\Delta_b + \chi)$ of mode a is taken for satisfying the single-photon resonance condition. The other parameters used are $\chi/\Delta_b = 0.001$, $\gamma_a/\Delta_b = 0.05$, $\bar{n}_a = 0$, and $\Omega_a/\gamma_a = 0.1$.

equation of motion $\dot{U}_{\text{app}}(t) = -iH_{\text{app}}^{(I)}(t)U_{\text{app}}(t)$, under the initial condition $U_{\text{app}}(0) = I$. Using the Magnus expansion, the solution for $U_{\text{app}}(t)$ can be obtained as

$$U_{\text{app}}(t) = \exp\left\{ i\frac{g_0^2}{\Delta_b^2}[\Delta_b t - \sin(\Delta_b t)]a^\dagger a a^\dagger a \right\}$$
$$\times \exp\left\{ \frac{g_0}{\Delta_b}a^\dagger a[b^\dagger(e^{i\Delta_b t} - 1)e^{i\theta} \right.$$
$$\left. - b(e^{-i\Delta_b t} - 1)e^{-i\theta}] \right\}. \tag{32}$$

This unitary operator is a conditional displacement operator for mode b, where the displacement is proportional to the excitation number m in mode a: $a^\dagger a|m\rangle_a = m|m\rangle_a$. The displacement amplitude (the maximum displacement) induced by a single photon is $2g_0/\Delta_b$. When $g_0/\Delta_b > 1$, the coherent state $|\eta'(t)\rangle_b$ [cf., Eq. (14) for $m = 1$] can be approximately distinguished from the vacuum state $|0\rangle_b$. The displacement of mode b induced by a single photon can be seen by calculating the dynamics of the average excitation $\langle n_b(t)\rangle = \langle b^\dagger b\rangle = |\eta'(t)|^2$ in mode b when the system is initially in the state $|1\rangle_a|0\rangle_b$. In Fig. 7, we show the dynamics of $\langle n_b(t)\rangle$ for several values of $|\beta_{ss}|$ in the presence of dissipations. These plots show that a larger displacement amplitude can be obtained for a larger $|\beta_{ss}|$, and that the dissipations will decrease the amplitude of the displacement. In the inset, we
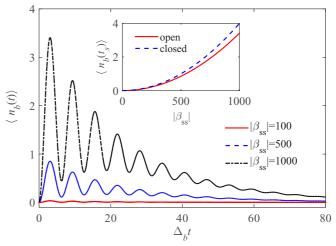

FIG. 7. The dynamics of the average excitation number $\langle n_b(t)\rangle$ in mode b when $\chi/\Delta_b = 0.001$ and the enhanced factor takes various values $|\beta_{ss}| = 100$, 500, and 1000. The inset shows the average excitation number $\langle n_b(t_s)\rangle$ at time $t_s = \pi/\Delta_b$ as a function of $|\beta_{ss}|$ in both the closed- and open-system cases. The other parameters used are $\gamma_a/\Delta_b = \gamma_b/\Delta_b = 0.05$ and $\bar{n}_a = \bar{n}_b = 0$.

plot the variable $\langle n_b(t_s)\rangle$, which corresponds to the maximal displacement η_{max}, as a function of $|\beta_{ss}|$. We see that the maximal displacement could be larger than the zero-point fluctuation of mode b (i.e., $\langle n_b\rangle > 1$). This means that the conditional displacement dynamics of the system can be used to create quantum superposition of macroscopically distinct states in mode b.

We see clearly from the unitary evolution operator (32) that the displacement of mode b depends on the photon number m in mode a. To create the Schrödinger cat states for mode b, we assume that the initial state of the system is

$$|\Psi(0)\rangle = \frac{1}{\sqrt{2}}(|0\rangle_a + |1\rangle_a)|0\rangle_b. \tag{33}$$

Then in terms of the unitary evolution operator (31) we can obtain the state of the system at time t as

$$|\Psi(t)\rangle = \frac{1}{\sqrt{2}}[|0\rangle_a|0\rangle_b + \exp[i\vartheta''(t)]|1\rangle_a|\eta''(t)\rangle_b], \tag{34}$$

where the phase and displacement amplitude are defined by

$$\vartheta''(t) = \frac{g_0^2}{\Delta_b^2}[\Delta_b t - \sin(\Delta_b t)] - \omega_a' t,$$
$$\eta''(t) = \frac{g_0}{\Delta_b}(1 - e^{-i\Delta_b t})e^{i\theta}. \tag{35}$$

We see that the displacement reaches its maximum $\eta''_{\text{max}} = 2g_0 e^{i\theta}/\Delta_b$ at time $\Delta_b t = (2n + 1)\pi$ for natural numbers n.

To create quantum superposition of mode b, we measure the state of mode a with the bases $|\pm\rangle_a = (|0\rangle_a \pm |1\rangle_a)/\sqrt{2}$. If we express the state of mode a with the basis states $|\pm\rangle_a$, then the state of the system becomes

$$|\Psi(t)\rangle = \frac{1}{2}[|+\rangle_a(|0\rangle_b + e^{i\vartheta''(t)}|\eta''(t)\rangle_b)$$
$$+ |-\rangle_a(|0\rangle_b - e^{i\vartheta''(t)}|\eta''(t)\rangle_b)]. \tag{36}$$
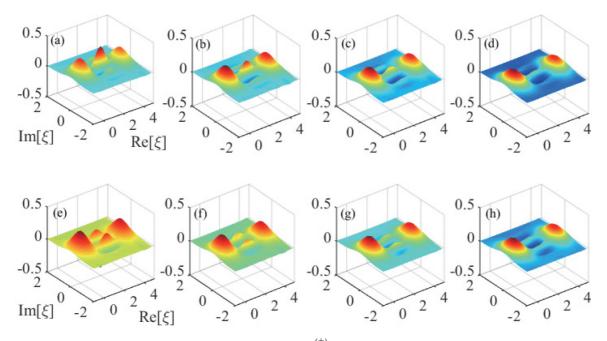
FIG. 8. Plots of Wigner functions $W_{\rho_b^{(\pm)}}(\xi)$ of the generated states $\rho_b^{(\pm)}(t_s)$ when the decay rates take different values: (a), (e) $\gamma_a/\Delta_b = \gamma_b/\Delta_b = 0$; (b), (f) $\gamma_a/\Delta_b = \gamma_b/\Delta_b = 0.05$; (c), (g) $\gamma_a/\Delta_b = \gamma_b/\Delta_b = 0.1$; and (d), (h) $\gamma_a/\Delta_b = \gamma_b/\Delta_b = 0.5$. The Wigner functions in the first and second rows correspond to the states $\rho_b^{(+)}$ and $\rho_b^{(-)}$, respectively. The other parameters are given by $\chi/\Delta_b = 0.001$, $\beta = 2000$, $\bar{n}_a = \bar{n}_b = 0$, and $t_s = \pi/(\Delta_b + \chi)$.

Corresponding to the states $|\pm\rangle_a$ are measured, the mode b will collapse into the states

$$|\phi_\pm(t)\rangle_b = \mathcal{N}_\pm(|0\rangle_b \pm e^{i\vartheta''(t)}|\eta''(t)\rangle_b), \tag{37}$$

where the normalization constants are defined by

$$\mathcal{N}_\pm = \left[2\left(1 \pm e^{-\frac{|\eta''(t)|^2}{2}}\cos\vartheta''(t)\right)\right]^{-1/2}. \tag{38}$$

The corresponding probabilities for the measured states $|\pm\rangle_a$ are

$$P_\pm(t) = \tfrac{1}{2}\left[1 \pm e^{-\frac{|\eta''(t)|^2}{2}}\cos\vartheta''(t)\right], \tag{39}$$

which are approximated as $1/2$ when $|\eta''(t)| \gg 1$.

In numerical simulations, we consider the transformed Hamiltonian H_{tra} and include the dissipations of the two modes. By numerically solving the quantum master equation (5) and performing the measurement at time $t_s = \pi/\Delta_b$, we can obtain two density matrices of mode b corresponding to the two measurement states $|\pm\rangle$ of mode a. By expressing the density matrix of the two-mode system as Eq. (18), we can solve the equations of motion for these density-matrix elements, and then obtain the density matrix $\rho'(t)$. We proceed performing the measurement of mode a into the states $|\pm\rangle_a$. After the measurement, we obtain the density matrices $\rho_b^{(\pm)}(t_s)$ of mode b. Then we can calculate the Wigner functions for the density matrices $\rho_b^{(\pm)}$ based on the definition of the Wigner function for a density matrix ρ_b [47]:

$$W(\xi) = \frac{2}{\pi}\text{Tr}[D_b^\dagger(\xi)\rho_b D_b(\xi)(-1)^{b^\dagger b}], \tag{40}$$

where ξ is a complex variable and $D_b(\xi) = \exp(\xi b^\dagger - \xi^* b)$ is the usual displacement operator for mode b.

In Fig. 8, we plot the Wigner functions $W_{\rho_b^{(\pm)}}(\xi)$ of the generated states $\rho_b^{(\pm)}(t_s)$ in mode b when the decay rates take different values: Figs. 8(a) and 8(e) $\gamma_a/\Delta_b = 0$, Figs 8(b) and 8(f) $\gamma_a/\Delta_b = 0.05$, Figs 8(c) and 8(g) $\gamma_a/\Delta_b = 0.1$, and Figs. 8(d) and 8(h) $\gamma_a/\Delta_b = 0.5$. Figures 8(a)–8(d) and 8(e)–8(h) are plotted for the states $\rho_b^{(+)}$ and $\rho_b^{(-)}$, respectively. Here we can see that the Wigner functions exhibit clear evidence of macroscopically distinct superposition components and quantum interference pattern. With the increase of the decay rate, the interference pattern disappears gradually, and the main peak corresponding to the coherent component $|\eta''\rangle$ moves toward the origin; this is because the coherent state decays to the vacuum state in the presence of dissipation.

We also study the influence of the thermal occupation number in mode b on the cat state generation. This consideration makes sense in the case where the mode b is a mechanical resonator and hence the thermal occupation number cannot be neglected. Usually, for mechanical mode b, the decay rate γ_b is smaller than that (γ_a) of the electromagnetic mode a. In Fig. 9, we plot the Wigner functions $W_{\rho_b^{(\pm)}}(\xi)$ of the states $\rho_b^{(\pm)}(t_s)$ when the thermal occupation number takes different values: Figs. 9(a) and 9(e) $\bar{n}_b = 1$, Figs. 9(b) and 9(f) $\bar{n}_b = 3$, Figs. 9(c) and 9(g) $\bar{n}_b = 5$, and Figs. 9(d) and 9(h) $\bar{n}_b = 8$. The panels in the first and second rows correspond to states $\rho_b^{(+)}$ and $\rho_b^{(-)}$, respectively. We can see that the interference phenomenon (i.e., the oscillation between the main peaks) disappears gradually with the increase of the thermal occupation number $\bar{n}_b$.

VI. GEOMETRICAL QUANTUM OPERATION

In this section, we show that a Kerr interaction of mode a can be implemented in a geometric manner and that this
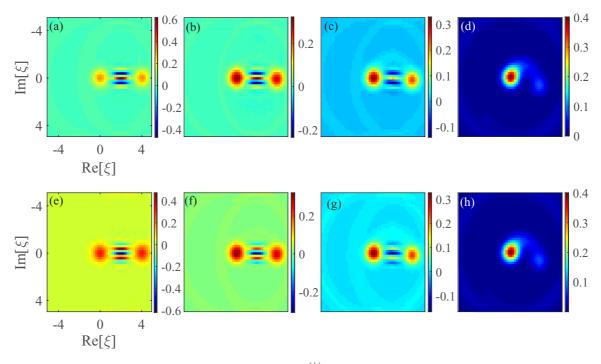
FIG. 9. Plots of Wigner functions $W_{\rho_b^{(\pm)}}(\xi)$ of the generated states $\rho_b^{(\pm)}(t_s)$ when the thermal excitation number take different values: (a), (e) $\bar{n}_b = 1$; (b), (f) $\bar{n}_b = 3$; (c), (g) $\bar{n}_b = 5$; and (d), (h) $\bar{n}_b = 8$. The Wigner functions in the first and second rows correspond to states $\rho_b^{(+)}$ and $\rho_b^{(-)}$, respectively. The other parameters are given by $\chi/\Delta_b = 0.001$, $\beta = 2000$, $\gamma_a/\Delta_b = 0.05$, $\gamma_b/\Delta_b = 0.01$, $\bar{n}_a = 0$, and $t_s = \pi/(\Delta_b + \chi)$.

geometric operation can be used to generate the Schrödinger cat and kitten states.

A. Geometrically induced Kerr interaction

The quadrature operator in the generalized optomechanical-like interaction can be used to implement geometric quantum operation of mode a by using the method of unconventional geometric phase. In this section, we study how to create a self-Kerr nonlinear interaction of mode a by designing a sequence of unitary operations. To this end, we consider the resonant driving case ($\Delta_b = 0$) of mode b, in which the Hamiltonian becomes

$$H_{\text{res}} = \omega'_a a^\dagger a - g_0 a^\dagger a (b^\dagger e^{i\theta} + b e^{-i\theta}). \quad (41)$$

The unitary evolution operator associated with this resonant driving Hamiltonian H_{res} is given by

$$U(t, \theta) = e^{-i\omega'_a t a^\dagger a} e^{i g_0 t a^\dagger a (b^\dagger e^{i\theta} + b e^{-i\theta})}. \quad (42)$$

Here, the phase angle θ is an important parameter for realization of the geometric operation. Concretely, a self-Kerr interaction for mode a can be obtained by implementing a chain of unitary evolution [48] as

$$\begin{aligned} U_{\text{tot}} &= U(t, 3\pi/2)U(t, \pi)U(t, \pi/2)U(t, 0) \\ &= \exp[-i\theta(t)a^\dagger a] \exp\left[2i g_0^2 t^2 (a^\dagger a a^\dagger a - a^\dagger a)\right], \quad (43) \end{aligned}$$

with $\theta(t) = 4\omega'_a t - 2g_0^2 t^2$. Note that the present geometric scheme can also be used to study the Planck-scale physics [49], and that the geometric operation in pulsed optomechanics [50] has been used to generation of nonclassical mechanical states [51].

The unitary evolution operator U_{tot} represents a pure self-Kerr interaction of mode a, and it is different from the transformed Kerr nonlinearity $U_{\text{app}}(t)$ associated with the optomechanical coupling H_{app}. The pure self-Kerr interaction is independent of the phonon states and hence the two modes are decoupled from each other with no phonon sidebands. However, in the optomechanical interactions, the eigenstates are the number states for mode a dressed by the displaced number states for mode b [6]. Moreover, the phase shift associated with the Kerr interaction $2g_0^2 t^2$ is continuously tunable and it can reach π which is needed for realization of logic gates for quantum computation. The Kerr interaction in $U_{\text{app}}(t)$ only works at time $t = 2n\pi/\Delta_b$.

B. Generation of the Schrödinger cat and kitten states

The geometric Kerr interaction can be used to create the Schrödinger cat and kitten states [52,53] in mode a. To generate the Schrödinger cat states, we assume that the initial state of mode a is $|\alpha\rangle = e^{-\frac{|\alpha|^2}{2}} \sum_{n=0}^{\infty} \frac{\alpha^n}{\sqrt{n!}} |n\rangle$, then, up to a free evolution $\exp(-4i\omega'_a t a^\dagger a)$, the state of the system at time t becomes

$$|\psi(\tau)\rangle_a = e^{-\frac{|\alpha|^2}{2}} \sum_{n=0}^{\infty} \frac{\alpha^n}{\sqrt{n!}} e^{i\frac{\tau}{2}n(n-1)} |n\rangle_a, \quad (44)$$

where we introduce $\tau = 4g_0^2 t^2$. Since $n(n-1)$ is an even number, then we know that $|\Psi(\tau + 2\pi)\rangle$ is a periodic function of τ with the period $T = 2\pi$, $|\psi(\tau + 2\pi)\rangle_a = |\psi(\tau)\rangle_a$. Moreover, based on this relation $e^{i\frac{\tau}{2}(n+2N)(n+2N-1)} = e^{i\frac{\tau}{2}n(n-1)} e^{i\tau N(2N+2n-1)}$, we can see that if we choose the $\tau =$

$2\pi M/N$, then the state can be expressed as

$$|\psi(MT/N)\rangle_a = \sum_{k=0}^{2N-1} c_k |\alpha e^{i\varphi_k}\rangle_a, \tag{45}$$

where $|\alpha e^{i\varphi_k}\rangle_a$ are coherent states with the phase $\varphi_k = k\pi/N$ ($k = 0, 1, 2, \ldots, 2N-1$). The superposition coefficients are given by

$$c_k = \frac{1}{2N} \sum_{n=0}^{2N-1} e^{-i\frac{\pi}{N}[kn - Mn(n-1)]}. \tag{46}$$

The evolution time is $4t$ with $t = [\tau/(4g_0^2)]^{1/2} = [2M\pi/(4g_0^2 N)]^{1/2}$.

We now show two examples for the generation of the Schrödinger cat and kitten states. When $N = 2$ and $M = 1$, by calculating the above superposition coefficients and phase angles, we obtain the cat state as

$$|\psi_{\text{cat}}(\tau = \pi)\rangle_a = \frac{1}{\sqrt{2}}(e^{-i\pi/4}|i\alpha\rangle_a + e^{i\pi/4}|-i\alpha\rangle_a). \tag{47}$$

When $N = 3$ and $M = 1$, we obtain a kitten state with three superposition components as

$$|\psi_{\text{kitten}}(\tau = 2\pi/3)\rangle_a$$
$$= \frac{1}{\sqrt{3}}(e^{i\pi/6}|\alpha\rangle_a - i|\alpha e^{i2\pi/3}\rangle_a e^{i\pi/6}|\alpha e^{i4\pi/3}\rangle_a). \tag{48}$$

Note that the generation of Schrödinger cat states in an optomechanical cavity has been proposed using the dynamical method [54–56].

The generated Schrödinger cat state and kitten state can be characterized by plotting their Wigner functions. For mode a in the density matrix ρ_a, its Wigner function is defined by

$$W(\xi) = \frac{2}{\pi} \text{Tr}[D_a^\dagger(\xi)\rho_a D_a(\xi)(-1)^{a^\dagger a}], \tag{49}$$

where ξ is a complex variable and $D_a(\xi) = \exp(\xi a^\dagger - \xi^* a)$ is the usual displacement operator for mode a. Corresponding to the above two states $|\psi_{\text{cat}}(\tau = \pi)\rangle_a$ and $|\psi_{\text{kitten}}(\tau = 2\pi/3)\rangle_a$, their Wigner functions can be calculated as

$$W_{|\psi_{\text{cat}}(\tau=\pi)\rangle_a}(\xi) = \frac{1}{\pi}\left[e^{-2|\xi-i\alpha|^2} + e^{-2|\xi+i\alpha|^2} + 2e^{-2|\xi|^2}\sin[4\text{Re}(\alpha\xi^*)]\right], \tag{50}$$

and

$$W_{|\psi_{\text{kitten}}(\tau=2\pi/3)\rangle_a}(\xi) = \frac{2}{3\pi}\left\{e^{-2|\xi-\alpha|^2} + e^{-2|\xi-\alpha e^{i2\pi/3}|^2} + e^{-2|\xi-\alpha e^{i4\pi/3}|^2} + 2\text{Re}[-i\exp[i\text{Im}(\xi\alpha^* - \xi\alpha^* e^{-i2\pi/3})]e^{-i\pi/6}C_1\right.$$
$$\left. + \exp[i\text{Im}(\xi\alpha^* - \xi\alpha^* e^{-i4\pi/3})]C_2 + i\exp[i\text{Im}(\xi\alpha^* e^{-i2\pi/3} - \xi\alpha^* e^{-i4\pi/3})]e^{i\pi/6}C_3]\right\}, \tag{51}$$

where $C_1 = {}_a\langle\xi - \alpha|-\xi + \alpha e^{i2\pi/3}\rangle_a$, $C_2 = {}_a\langle\xi - \alpha|-\xi + \alpha e^{i4\pi/3}\rangle_a$, and $C_3 = {}_a\langle\xi - \alpha e^{i2\pi/3}|-\xi + \alpha e^{i4\pi/3}\rangle_a$ are the overlaps between coherent states which can be calculated by using the formula $\langle\alpha|\beta\rangle = \exp(-|\alpha|^2/2 + \beta\alpha^* - |\beta|^2/2)$.

In Fig. 10, we show the two Wigner functions when the coherent amplitude is taken as $\alpha = 2$. Here we can see that there are two and three main peaks, which correspond to the two and three superposition components in the two states $|\psi_{\text{cat}}(\tau = \pi)\rangle_a$ and $|\psi_{\text{kitten}}(\tau = 2\pi/3)\rangle_a$, defined in Eqs. (47) and (48), respectively. These main peaks can be well resolved because the magnitude of the coherent-state components is sufficiently large. For generation of quantum superposition

of macroscopically distinct states, the coherent amplitudes of superposed coherent states usually should be larger than two. Moreover, in the areas between these main peaks, we can see some oscillation pattern, which is the signature of quantum superposition.

To evaluate the influence of the dissipations on the geometrical state generation, we need to solve four quantum master equations corresponding to the four steps of evolution (with different Hamiltonians). However, here we adopt the quantum trajectory method instead of the quantum mater equation in our simulations. This is because the dimension of the Hilbert space is too large to be calculated with our computational resource. For the master-equation method, the number of the equations of motion is the square of the dimension of the total system. Instead, by using the quantum trajectory method, the number of the equations of motion is largely decreased because it is equal to the dimension of the total Hilbert space. For the zero-temperature-environment case, the system can be described by a non-Hermite Hamiltonian by adding two imaginary terms phenomenologically as follows:

$$H^{(l=1-4)} = \omega_a' a^\dagger a - g_0 a^\dagger a(b^\dagger e^{i\theta_l} + b e^{-i\theta_l})$$
$$- i\frac{\gamma_a}{2} a^\dagger a - i\frac{\gamma_b}{2} b^\dagger b, \tag{52}$$

where the phase angles are taken as $\theta_1 = 0, \theta_2 = \pi/2, \theta_3 = \pi$, and $\theta_4 = 3\pi/2$. Using these Hamiltonians, we can numerically solve the Schrödinger equations step by step, then we obtain the final state of the system. Based on the reduced
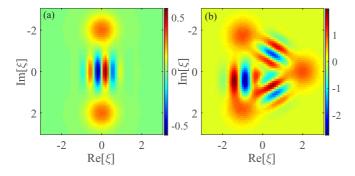

FIG. 10. Plots of the Wigner functions defined in Eqs. (50) and (51), of the cat state $\psi(\tau = \pi)$ and the kitten state $|\psi(\tau = 2\pi/3)\rangle$ defined in Eqs. (47) and (48), respectively. Here the coherent amplitude of the initial coherent state $|\alpha\rangle$ is $\alpha = 2$.
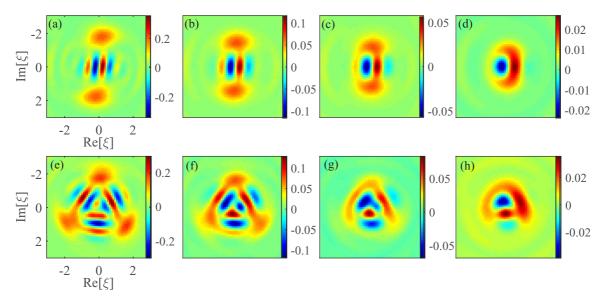
FIG. 11. The Wigner functions correspond to the generated cat state and the kitten state in the open system case. Here panels (a)–(d) are the Wigner functions for the Schrödinger cat state with two superposition components, and panels (e)–(h) are the Wigner functions for the Schrödinger kitten state with three superposition components. The decay rates in these panels from left to right are given by $\gamma_a/\Delta_b = \gamma_b/\Delta_b = 0.01, 0.05, 0.1,$ and 0.2. The coherent amplitude in the initial state $|\alpha\rangle$ is $\alpha = 2$. Since the ω'_a term only introduces a rotation in the phase space, the shape of the Wigner function is independent of ω'_a. The other parameters are given by $\chi/\Delta_b = 0.001, |\beta_{ss}| = 1000$, and $\bar{n}_a = \bar{n}_b = 0$.

density matrix of mode a, we can calculate the Wigner function of the state of mode a.

In Fig. 11 we plot the Wigner functions of the two- and three-component superposition states when the decay rates of the two modes take different values. Here, Figs. 11(a)–11(d) correspond to the Wigner functions of the cat state in the open-system case, while Figs. 11(e)–11(h) correspond to the Wigner functions of the kitten state in the open-system case. We can see that with the increase of the decay rate, the quantum interference evidence in the Wigner function disappears gradually. Therefore, the dissipation of the two modes will harm the quantum interference effect in the generated Schrödinger cat and kitten states.

VII. DISCUSSION OF EXPERIMENTAL IMPLEMENTATION

Finally, we present a discussion of the experimental implementation of this scheme. The main result in this work is the realization of a generalized ultrastrong optomechanical-like coupling in a cross-Kerr-type coupled two-mode system, in which one of the two modes is driven by a monochromatic field. As a result, the nominated physical systems should contain a cross-Kerr interaction, and one of the two modes should be driven by a monochromatic field. In addition, the parameter condition for this scheme is that the cross-Kerr parameter should be much smaller than the driving detuning Δ_b of mode b such that the approximation used in discarding the cross-Kerr term in the transformed Hamiltonian is justified. For observing some quantum nonlinear effects in the ultrastrong-coupling regime, we need a relatively large displacement amplitude $|\beta_{ss}|$ ($\approx 10^3$ in our simulations) to enhance the generalized optomechanical-like coupling. Lastly, for resolving some sideband effects induced by mode b, the sideband-resolution condition $\Delta_b \gg \gamma_a$ should be satisfied.

Therefore, the parameter conditions for implementation of this scheme are given by

$$\Delta_b \gg \chi, \quad \Delta_b \gg \gamma_a, \quad g_0 \sim \Delta_b. \qquad (53)$$

Note that the generalized optomechanical-like coupling strength g_0 should be much larger than the decay rate γ_a of mode a, and the cross-Kerr interaction strength χ could be either larger or smaller than the decay rate γ_a. This relaxed condition of the cross-Kerr interaction raises the possibility for implementation of this scheme with many quantum optical systems. In addition, since the driving detuning Δ_b (playing the role of the effective frequency of mode b in the displacement representation) is a controllable parameter by choosing a proper driving frequency ω_{Lb}, then we can design a proper Δ_b such that the relations $\Delta_b \gg \chi$ and $\Delta_b \gg \gamma_a$ are satisfied. We also choose a proper driving amplitude Ω_b such that the displacement amplitude $|\beta_{ss}|$ is large enough to confirm the relation $g_0 \sim \Delta_b$.

In principle, our method is general and hence it can be implemented in various cross-Kerr-type coupled two-mode systems. In quantum optics, the cross-Kerr interaction between two bosonic modes is usually obtained by coupling these two modes to a common medium, which could be a three-level atom [24], an "N"-type atom [25–28,57], and an "M"-type atom [29], where the atom could be either a natural or an artificial atom, which corresponds to cavity QED [30] or circuit QED [58–63]. The implementation of the cross-Kerr interaction can also be realized in optomechanical systems [64–67] and in a coupled cavity-ion system [68,69]. Some proposals on the cross-Kerr interaction are based on the system consisting of two continuous-wave optical fields coupled to an ensemble of atoms with an "N"-type configuration [25–28]. This method also works for the cavity field case and hence a cross-Kerr interaction between two cavity fields can be obtained. For optical cavity modes, the

TABLE I. Parameters of the cross-Kerr-type coupled systems reported in literature: the resonance frequencies ω_a and ω_b of modes a and b, the cross-Kerr interaction strength χ, the decay rates γ_a and γ_b for modes a and b, the thermal excitation occupations $\bar{n}_a$ and $\bar{n}_b$ in the baths of modes a and b. Here the subscripts "E" and "T" of the reference number denote the reference as an experimental work and a theoretical work, respectively.

Ref.	Description	$\omega_a/(2\pi)$ (GHz)	$\omega_b/(2\pi)$ (GHz)	$\chi/(2\pi)$ (kHz)	$\gamma_a/(2\pi)$ (kHz)	$\gamma_b/(2\pi)$ (kHz)	$\bar{n}_a$	$\bar{n}_b$
[62]$_E$	Circuit-QED	8.493	9.32	2.59×10^3	1.25	5.25	≈ 0	≈ 0
[58]$_T$, [63]	Circuit-QED	≈ 5	≈ 5	2.5×10^3	$\approx 30 \times 10^3$	$\approx 30 \times 10^3$	≈ 0	≈ 0
[65]$_E$	Quadratic optomech.	282×10^3	0.134×10^{-3}	0.395×10^{-4}	5.94×10^2	0.122×10^{-3}	≈ 0	46648
[68]$_T$, [69]	Cavity-ion system	351×10^3	$\gg 15.1 \times 10^{-3}$	0.796	41.7		≈ 0	

resonance frequencies ($\approx 10^{14}$ Hz) are much larger than the decay rates ($\approx 10^7$ Hz), and the thermal occupation numbers are negligible. In typical optical-cavity-QED systems, the atom-field coupling strength is of the order of 10^8 Hz [30]. Since the cross-Kerr interaction is of the order of the atom-field coupling strength times the cubic order of a small ratio (the effective coupling is obtained by adiabatically eliminating the atom coherence, the value of the ratio is much smaller than one, for example 10^{-1}) [58], then the effective cross-Kerr parameter could be of the order of 10^4–10^5 Hz. For microwave field modes, the resonance frequencies might be of the order of 5–10 GHz and the decay rates are 10^4–10^5 Hz. The thermal occupation numbers are negligible at the temperature around 20 mK. The cross-Kerr parameters are of the order of 10^6 Hz.

For the purpose of comparison, we list in Table I some relating parameters reported in either theoretical proposals or realistic experiments concerning the two-mode cross-Kerr-type-coupled systems. Note that great advances have been made in circuit QED [58–63]. From Table I we can see that, depending on the task, the coupled two-mode systems can be designed to have a wide range of parameters. It should be pointed out that, although our method also works for a weak cross-Kerr interaction case, we need a very large displacement β_{ss} to obtain an ultrastrong optomechanical-like coupling for an extremely weak cross-Kerr interaction (for example, in quadratic optomechanical systems), which means that a strong driving on mode b should be implemented. This might lead to an unwanted heating problem in experiments. In addition, for the coupled cavity-ion system, although the

cross-Kerr interaction has been studied theoretically [68], the experimental implementation of the cross-Kerr interaction between the cavity field and the vibrational mode has not been reported. Therefore, the circuit-QED systems might be a promising platform for realizing the present scheme. In this case, the two modes of the optomechanical-like interaction are electromagnetic fields.

Based on the above discussion, in Table II we suggest some parameters for simulation of this scheme. In our model, the involved parameters include the resonance frequencies ω_a and ω_b, the cross-Kerr interaction strength χ, the decay rates of the two bosonic modes γ_a and γ_b, dimensionless displacement amplitude $|\beta_{ss}|$, the driving amplitude Ω_b and frequency ω_{Lb} of mode b. Below we analyze the feasibility of our scheme based on the above listed parameters. Mode a could be either optical or microwave mode. In the cat state generation tasks, the free Hamiltonian of mode a will not affect the dynamics of the system, because it commutes the other terms in the Hamiltonian. For the photon blockade task, the single-photon resonance is taken and then useful parameter is the driving detuning $\Delta_a = \omega_a - \omega_{La}$. For optical mode a, its frequency is of the order of hundreds of terahertz, the decay rate might be $\gamma_a \approx 2\pi \times 10$–100 MHz. For microwave mode a, its frequency might be $\omega_a \approx 2\pi \times 5$–10 GHz, the decay rate might be $\gamma_a \approx 2\pi \times 100$ kHz. The cross-Kerr interaction between the two modes is of the order of 1–10 kHz [62]. By choosing proper driving amplitude and frequency, the system can work in the ultrastrong-coupling regime.

TABLE II. The parameters used in our simulations: the resonance frequency $\omega_a' = \omega_a + \chi |\beta_{ss}|^2$ of mode a, the driving detuning (the effective frequency in the transformed representation) $\Delta_b = \omega_b - \omega_{Lb}$ of mode b, the cross-Kerr interaction strength χ, the displacement amplitude $|\beta_{ss}|$, the single-photon optomechanical-coupling strength $g_0 = \chi |\beta_{ss}|$, the decay rates γ_a and γ_b of modes a and b, the thermal occupation numbers $\bar{n}_a$ and $\bar{n}_b$ in the baths of modes a and b, and the single-photon strong-coupling condition g_0/γ_a.

Notation	Remarks	Scaled parameters	Parameters
ω_a'	Arbitrary		
Δ_b	As the frequency scales	1	$2\pi \times 1$ MHz
χ	$\chi/\Delta_b \ll 1$ for approximation	$\chi/\Delta_b = 0.001$–0.01	$2\pi \times (1$–10) kHz
$|\beta_{ss}|$	$|\beta_{ss}| \gg 1$ for coupling enhancement		1000–2000 or 100–200
$g_0 = \chi |\beta_{ss}|$	Enhanced optomechanical-coupling strength	$g_0/\Delta_b \approx 1$–2	$2\pi \times (1$–2) MHz
γ_a	Decay rate of mode a	$\gamma_a/\Delta_b = 0.01$–0.1	$2\pi \times (10$–100) kHz
γ_b	Decay rate of mode b	$\gamma_b/\Delta_b = 0.01$–0.1	$2\pi \times (10$–100) kHz
$\bar{n}_a$	Negligible for optical and microwave fields		0
$\bar{n}_b$	A finite number for a mechanical resonator		0–10
g_0/γ_a	Single-photon strong-coupling condition	10–200	

VIII. CONCLUSIONS

In conclusion, we proposed the concept of a generalized ultrastrong-optomechanical-like coupling by replacing the position operator in the radiation-pressure coupling with a rotated quadrature operator. This generalization will provide an additional dimension for manipulation of the optomechanical interaction because the rotated quadrature operator is an additional controllable degree of freedom. We also proposed a reliable physical scheme to realize this generalized interaction in a quantum optical model which consists of two bosonic modes coupled through a cross-Kerr interaction. By using the transformation method in the quantum master equation, we derived an approximate Hamiltonian and presented the detailed parameter conditions under which the approximate Hamiltonian is valid. Some applications of this generalized optomechanical-like interactions were proposed. These include the photon blockade effect, the cat-state generation, and the implementation of geometric operation. This proposal provides a reliable method for studying few-photon optomechanics or simulating the optomechanical-type interactions between two electromagnetic fields with current experimental techniques.

[1] T. J. Kippenberg and K. J. Vahala, Cavity optomechanics: Back-action at the mesoscale, Science **321**, 1172 (2008).

[2] M. Aspelmeyer, P. Meystre, and K. Schwab, Quantum optomechanics, Phys. Today **65**(7), 29 (2012).

[3] M. Aspelmeyer, T. J. Kippenberg, and F. Marquardt, Cavity optomechanics, Rev. Mod. Phys. **86**, 1391 (2014).

[4] A. Nunnenkamp, K. Børkje, and S. M. Girvin, Single-Photon Optomechanics, Phys. Rev. Lett. **107**, 063602 (2011).

[5] P. Rabl, Photon Blockade Effect in Optomechanical Systems, Phys. Rev. Lett. **107**, 063601 (2011).

[6] J.-Q. Liao, H. K. Cheung, and C. K. Law, Spectrum of single-photon emission and scattering in cavity optomechanics, Phys. Rev. A **85**, 025803 (2012).

[7] J.-Q. Liao and C. K. Law, Correlated two-photon scattering in cavity optomechanics, Phys. Rev. A **87**, 043809 (2013).

[8] T. Hong, H. Yang, H. Miao, and Y. Chen, Open quantum dynamics of single-photon optomechanical devices, Phys. Rev. A **88**, 023812 (2013).

[9] X.-W. Xu, Y.-J. Li, and Y.-x. Liu, Photon-induced tunneling in optomechanical systems, Phys. Rev. A **87**, 025803 (2013).

[10] W. Marshall, C. Simon, R. Penrose, and D. Bouwmeester, Towards Quantum Superpositions of a Mirror, Phys. Rev. Lett. **91**, 130401 (2003).

[11] J.-Q. Liao and L. Tian, Macroscopic Quantum Superposition in Cavity Optomechanics, Phys. Rev. Lett. **116**, 163602 (2016).

[12] A. Xuereb, C. Genes, and A. Dantan, Strong Coupling and Long-Range Collective Interactions in Optomechanical Arrays, Phys. Rev. Lett. **109**, 223601 (2012).

[13] A. J. Rimberg, M. P. Blencowe, A. D. Armour, and P. D. Nation, A cavity-Cooper pair transistor scheme for investigating quantum optomechanics in the ultra-strong coupling regime, New J. Phys. **16**, 055008 (2014).

[14] T. T. Heikkilä, F. Massel, J. Tuorila, R. Khan, and M. A. Sillanpää, Enhancing Optomechanical Coupling via the Josephson Effect, Phys. Rev. Lett. **112**, 203603 (2014).

[15] J.-M. Pirkkalainen, S. U. Cho, F. Massel, J. Tuorila, T. T. Heikkilä, P. J. Hakonen, and M. A. Sillanpää, Cavity optomechanics mediated by a quantum two-level system, Nat. Commun. **6**, 6981 (2015).

[16] J.-Q. Liao, K. Jacobs, F. Nori, and R. W. Simmonds, Modulated electromechanics: Large enhancements of nonlinearities, New J. Phys. **16**, 072001 (2014).

[17] X.-Y. Lü, Y. Wu, J. R. Johansson, H. Jing, J. Zhang, and F. Nori, Squeezed Optomechanics with Phase-Matched Amplification and Dissipation, Phys. Rev. Lett. **114**, 093602 (2015).

[18] P.-B. Li, H.-R. Li, and F.-L. Li, Enhanced electromechanical coupling of a nanomechanical resonator to coupled superconducting cavities, Sci. Rep. **6**, 19065 (2016).

[19] M.-A. Lemonde, N. Didier, and A. A. Clerk, Enhanced nonlinear interactions in quantum optomechanics via mechanical amplification, Nat. Commun. **7**, 11338 (2016).

[20] Z. Wang and A. H. Safavi-Naeini, Enhancing a slow and weak optomechanical nonlinearity with delayed quantum feedback, Nat. Commun. **8**, 15886 (2017).

[21] M. Ludwig, B. Kubala, and F. Marquardt, The optomechanical instability in the quantum regime, New J. Phys. **10**, 095013 (2008).

[22] J. Qian, A. A. Clerk, K. Hammerer, and F. Marquardt, Quantum Signatures of the Optomechanical Instability, Phys. Rev. Lett. **109**, 253601 (2012).

[23] F. A. M. de Oliveira, M. S. Kim, P. L. Knight, and V. Buek, Properties of displaced number states, Phys. Rev. A **41**, 2645 (1990).

[24] T. Liu, Y. Zhang, B.-Q. Guo, C.-S. Yu, and W.-N. Zhang, Circuit QED: Cross-Kerr effect induced by a superconducting qutrit without classical pulses, Quantum Inf. Process. **16**, 209 (2017).

[25] H. Schmidt and A. Imamoğlu, Giant Kerr nonlinearities obtained by electromagnetically induced transparency, Opt. Lett. **21**, 1936 (1996).

[26] H. Kang and Y. Zhu, Observation of Large Kerr Nonlinearity at Low Light Intensities, Phys. Rev. Lett. **91**, 093601 (2003).

[27] G. F. Sinclair and N. Korolkova, Cross-Kerr interaction in a four-level atomic system, Phys. Rev. A **76**, 033803 (2007).

[28] G. F. Sinclair and N. Korolkova, Effective cross-Kerr Hamiltonian for a nonresonant four-level atom, Phys. Rev. A **77**, 033843 (2008).

[29] A. B. Matsko, I. Novikova, G. R. Welch, and M. S. Zubairy, Enhancement of Kerr nonlinearity by multiphoton coherence, Opt. Lett. **28**, 96 (2003).

[30] H. J. Kimble, Strong interactions of single atoms and photons in cavity QED, Phys. Scr. **1998**, 127 (1998).

[31] D. Hu, S.-Y. Huang, J.-Q. Liao, L. Tian, and H.-S. Goan, Quantum coherence in ultrastrong optomechanics, Phys. Rev. A **91**, 013812 (2015).

[32] M. Paternostro, M. S. Kim, and B. S. Ham, Generation of entangled coherent states via cross-phase-modulation in a double electromagnetically induced transparency regime, Phys. Rev. A **67**, 023811 (2003).

[33] L.-M. Kuang and L. Zhou, Generation of atom-photon entangled states in atomic Bose-Einstein condensate via electromagnetically induced transparency, Phys. Rev. A **68**, 043606 (2003).

[34] L.-M. Kuang, Z. B. Chen, and J. W. Pan, Generation of entangled coherent states for distant Bose-Einstein condensates via electromagnetically induced transparency, Phys. Rev. A **76**, 052324 (2007).

[35] G. J. Milburn, Quantum Optical Fredkin Gate, Phys. Rev. Lett. **62**, 2124 (1989).

[36] D. Vitali, M. Fortunato, and P. Tombesi, Complete Quantum Teleportation with a Kerr Nonlinearity, Phys. Rev. Lett. **85**, 445 (2000).

[37] P. Kok, W. J. Munro, K. Nemoto, T. C. Ralph, J. P. Dowling, and G. J. Milburn, Linear optical quantum computing with photonic qubits, Rev. Mod. Phys. **79**, 135 (2007).

[38] K. Nemoto and W. J. Munro, Nearly Deterministic Linear Optical Controlled-NOT Gate, Phys. Rev. Lett. **93**, 250502 (2004).

[39] N. Imoto, H. A. Haus, and Y. Yamamoto, Quantum nondemolition measurement of the photon number via the optical Kerr effect, Phys. Rev. A **32**, 2287 (1985).

[40] P. Grangier, J. A. Levenson, and J. P. Poizat, Quantum nondemolition measurements in optics, Nature (London) **396**, 537 (1998).

[41] S. Ding, G. Maslennikov, R. Hablützel, and D. Matsukevich, Cross-Kerr Nonlinearity for Phonon Counting, Phys. Rev. Lett. **119**, 193602 (2017).

[42] K. Xia, F. Nori, and M. Xiao, Cavity-Free Optical Isolators and Circulators Using a Chiral Cross-Kerr Nonlinearity, Phys. Rev. Lett. **121**, 203602 (2018).

[43] Our numerical results on the photon blockade are calculated based on the quantum optics toolbox by Tan [44], and some important data are checked with the QUTIP package [45,46].

[44] S. M. Tan, A computational toolbox for quantum and atomic optics, J. Opt. B: Quantum Semiclassical Opt. **1**, 424 (1999).

[45] J. R. Johansson, P. D. Nation, and F. Nori, QuTiP: An open-source Python framework for the dynamics of open quantum systems, Comput. Phys. Commun. **183**, 1760 (2012).

[46] J. R. Johansson, P. D. Nation, and F. Nori, QuTiP 2: A Python framework for the dynamics of open quantum systems, Comput. Phys. Commun. **184**, 1234 (2013).

[47] S. M. Barnett and P. M. Radmore, *Methods in Theoretical Quantum Optics* (Clarendon Press, Oxford, 1997).

[48] S.-L. Zhu and Z. D. Wang, Unconventional Geometric Quantum Computation, Phys. Rev. Lett. **91**, 187902 (2003).

[49] I. Pikovski, M. R. Vanner, M. Aspelmeyer, M. S. Kim, and Č. Brukner, Probing Planck-scale physics with quantum optics, Nat. Phys. **8**, 393 (2012).

[50] M. R. Vanner, I. Pikovski, G. D. Cole, M. S. Kim, Č. Brukner, K. Hammerer, G. J. Milburn, and M. Aspelmeyer, Pulsed quantum optomechanics, Proc. Natl. Acad. Sci. USA **108**, 16182 (2011).

[51] K. E. Khosla, M. R. Vanner, W. P. Bowen, and G. J. Milburn, Quantum state preparation of a mechanical resonator using an optomechanical geometric phase, New J. Phys. **15**, 043025 (2013).

[52] Z. Bialynicki-Birula, Properties of the generalized coherent state, Phys. Rev. **173**, 1207 (1968).

[53] A. Miranowicz, R. Tanaś, and S. Kielich, Generation of discrete superpositions of coherent states in the anharmonic oscillator model, Quantum Opt. **2**, 253 (1990.

[54] S. Mancini, V. I. Man'ko, and P. Tombesi, Ponderomotive control of quantum macroscopic coherence, Phys. Rev. A **55**, 3042 (1997).

[55] S. Bose, K. Jacobs, and P. L. Knight, Preparation of nonclassical states in cavities with a moving mirror, Phys. Rev. A **56**, 4175 (1997).

[56] S. Bose, K. Jacobs, and P. L. Knight, Scheme to probe the decoherence of a macroscopic object, Phys. Rev. A **59**, 3204 (1999).

[57] S. Rebić, J. Twamley, and G. J. Milburn, Giant Kerr Nonlinearities in Circuit Quantum Electrodynamics, Phys. Rev. Lett. **103**, 150503 (2009).

[58] Y. Hu, G.-Q. Ge, S. Chen, X.-F. Yang, and Y.-L. Chen, Cross-Kerr-effect induced by coupled Josephson qubits in circuit quantum electrodynamics, Phys. Rev. A **84**, 012329 (2011).

[59] S. E. Nigg, H. Paik, B. Vlastakis, G. Kirchmair, S. Shankar, L. Frunzio, M. H. Devoret, R. J. Schoelkopf, and S. M. Girvin, Black-Box Superconducting Circuit Quantization, Phys. Rev. Lett. **108**, 240502 (2012).

[60] J. Bourassa, F. Beaudoin, Jay M. Gambetta, and A. Blais, Josephson-junction-embedded transmission-line resonators: From Kerr medium to in-line transmon, Phys. Rev. A **86**, 013814 (2012).

[61] I. C. Hoi, A. F. Kockum, T. Palomaki, T. M. Stace, B. Fan, L. Tornberg, S. R. Sathyamoorthy, G. Johansson, P. Delsing, and C. M. Wilson, Giant Cross-Kerr Effect for Propagating Microwaves Induced by an Artificial Atom, Phys. Rev. Lett. **111**, 053601 (2013).

[62] E. T. Holland, B. Vlastakis, R. W. Heeres, M. J. Reagor, U. Vool, Z. Leghtas, L. Frunzio, G. Kirchmair, M. H. Devoret, M. Mirrahimi, and R. J. Schoelkopf, Single-Photon-Resolved Cross-Kerr Interaction for Autonomous Stabilization of Photon-Number States, Phys. Rev. Lett. **115**, 180501 (2015).

[63] J. Majer, J. M. Chow, J. M. Gambetta, Jens Koch, B. R. Johnson, J. A. Schreier, L. Frunzio, D. I. Schuster, A. A. Houck, A. Wallraff *et al.*, Coupling superconducting qubits via a cavity bus, Nature (London) **449**, 443 (2007).

[64] J. D. Thompson, B. M. Zwickl, A. M. Jayich, F. Marquardt, S. M. Girvin, and J. G. E. Harris, Strong dispersive coupling of

a high-finesse cavity to a micromechanical membrane, Nature (London) **452**, 72 (2008).

[65] J. C. Sankey, C. Yang, B. M. Zwickl, A. M. Jayich, and J. G. E. Harris, Strong and tunable nonlinear optomechanical coupling in a low-loss system, Nat. Phys. **6**, 707 (2010).

[66] M. Karuza, M. Galassi, C. Biancofiore, C. Molinelli, R. Natali, P. Tombesi, G. Di Giuseppe, and D. Vitali, Tunable linear and quadratic optomechanical coupling for a tilted membrane within an optical cavity: Theory and experiment, J. Opt. (Bristol, U. K.) **15**, 025704 (2013).

[67] Z. R. Gong, H. Ian, Y.-x. Liu, C. P. Sun, and F. Nori, Effective Hamiltonian approach to the Kerr nonlinearity in an optomechanical system, Phys. Rev. A **80**, 065801 (2009).

[68] F. L. Semião and A. Vidiella-Barranco, Effective cross-Kerr nonlinearity and robust phase gates with trapped ions, Phys. Rev. A **72**, 064305 (2005).

[69] C. Maurer, C. Becher, C. Russo, J. Eschner, and R. Blatt, A single-photon source based on a single Ca$^+$ ion, New J. Phys. **6**, 94 (2004).